

Deep searches for X-ray pulsations from Scorpius X-1 and Cygnus X-2 in support of continuous gravitational wave searches

Shanika Galaudage,^{1,2*} Karl Wette,^{3,2} Duncan K. Galloway,^{1,2} and Chris Messenger⁴

¹*School of Physics and Astronomy, Monash University, Clayton VIC 3800, Australia*

²*ARC Centre of Excellence for Gravitational Wave Discovery (OzGrav), Hawthorn VIC 3122, Australia*

³*Centre for Gravitational Astrophysics, Australian National University, Canberra ACT 2601, Australia*

⁴*SUPA, School of Physics and Astronomy, University of Glasgow, Glasgow G12 8QQ, United Kingdom*

Accepted XXX. Received YYY; in original form ZZZ

ABSTRACT

Neutron stars in low mass X-ray binaries are hypothesised to emit continuous gravitational waves that may be detectable by ground-based observatories. The torque balance model predicts that a higher accretion rate produces larger-amplitude gravitational waves, hence low mass X-ray binaries with high X-ray flux are promising targets for gravitational wave searches. The detection of X-ray pulsations would identify the spin frequency of these neutron stars, and thereby improve the sensitivity of continuous gravitational-wave searches by reducing the volume of the search parameter space. We perform a semi-coherent search for pulsations in the two low mass X-ray binaries Scorpius X-1 and Cygnus X-2 using X-ray data from the *Rossi X-ray Timing Explorer* Proportional Counter Array. We find no clear evidence for pulsations, and obtain upper limits (at 90% confidence) on the fractional pulse amplitude, with the most stringent being 0.034% for Scorpius X-1 and 0.23% for Cygnus X-2. These upper limits improve upon those of [Vaughan et al. \(1994\)](#) by factors of ~ 8.2 and ~ 1.6 respectively.

Key words: stars: neutron – X-rays: binaries – X-rays: Scorpius X-1 – X-rays: Cygnus X-2 – gravitational waves

1 INTRODUCTION

Accreting neutron stars in low mass X-ray binaries (LMXBs) can be spun up due to the transfer of angular momentum via accretion. The measured spin frequencies of accreting neutron stars (typically in the range 100–700 Hz) are significantly below the expected neutron star break-up limit of ~ 1000 Hz ([Cook et al. 1994](#)). This observation suggests that there must be some mechanism by which the angular momentum is transferred away from these systems, as typical accretion rates over their long accretion lifetimes would otherwise be sufficient to achieve maximal spin rates. A possible mechanism ([Bildsten 1998](#); [Chakrabarty et al. 2003](#)) is the emission of gravitational waves from a rapidly-rotating neutron star that deviates from axisymmetry (e.g. [Papaloizou & Pringle 1978](#); [Wagoner 1984](#)).

The frequency of the gravitational waves emitted by these sources is typically twice the spin frequency of the neutron star ([Van Den Broeck 2005](#)), and is modulated by the orbital motion of the star’s binary companion. The predicted strain is

$$h_0 \approx 3 \times 10^{-27} \frac{R_{10}^{3/4}}{M_{1.4}^{1/4}} \left(\frac{F_X}{10^8 \text{ erg cm}^{-2} \text{ s}^{-1}} \right)^{1/2} \left(\frac{1 \text{ kHz}}{\nu} \right)^{1/2}, \quad (1)$$

where M is the mass of the neutron star ($M_{1.4} = M/1.4 M_\odot$), R is

the radius of the neutron star ($R_{10} = R/10 \text{ km}$), F_X is the observed X-ray flux, and ν is the spin frequency of the neutron star ([Watts et al. 2008](#)). These gravitational waves are expected to be emitted persistently (e.g. [Prix 2009](#)) and are referred to as continuous gravitational waves (CWs). They are a potential target for current-generation gravitational wave observatories such as LIGO ([Aasi et al. 2015a](#)) and Virgo ([Acernese et al. 2015](#)), as well as for future ground-based detectors. Numerous searches for continuous gravitational waves from LMXBs have been performed to date ([Abbott et al. 2007a,b](#); [Aasi et al. 2015b](#); [Abbott et al. 2017a,b,c](#); [Meadors et al. 2017](#); [Abbott et al. 2019a,b](#); [Middleton et al. 2020](#)).

To search for continuous gravitational waves, we require a template describing the expected signal waveform. To construct such a template, we need information about the neutron star, such as its position in the sky and frequency evolution as a function of time. For neutron stars in binary systems, we additionally need to correct for the orbital motion of the system. Uncertainties in the orbital parameters result in a multiplicity of templates which must be searched to recover the true signal waveform. The greater the uncertainty in the binary system parameters, the larger the number of templates needed to search the parameter space at a given template resolution. For sufficiently large parameter spaces, the significant computational cost of the search requires the use of sub-optimal semi-coherent search strategies which sacrifice sensitivity for reduced computational cost (e.g. [Messenger 2011](#); [Leaci & Prix 2015](#)). Conversely,

* E-mail: shanika.galaudage@monash.edu

sufficiently precise constraints on the orbital parameters of the binary and spin frequency of the neutron star would reduce the search parameter space volume to a negligible number of templates and allow for an optimal fully-coherent search, thereby improving the sensitivity to a continuous wave signal.

The LMXBs Scorpius X-1 (Sco X-1) and Cygnus X-2 (Cyg X-2) are considered to be promising candidates for the detection of continuous gravitational waves. They have high X-ray fluxes ($\gtrsim 10^9$ erg cm $^{-2}$ s $^{-1}$) and precise constraints on the orbital period, radial velocities and epoch of inferior conjunction (Wang et al. 2018; Premachandra et al. 2016) which reduces the search parameter space. The spin frequency of these sources are unknown, however (Damle et al. 1988; Wood et al. 1991; Vaughan et al. 1994; Manchanda 2005). A measurement of the spin frequency would greatly reduce the parameter space volume of continuous gravitational wave searches targeting these neutron stars. A detection of X-ray pulsations would immediately provide such a measurement.

Searches for X-ray pulsations face similar challenges to continuous gravitational wave searches. These include accounting for the Doppler modulation of the signal phase due to the binary orbit; as a result, the computational cost of the search increases much more rapidly with observation time than does the gain in sensitivity (Messenger 2011; Leaci & Prix 2015), making a fully-coherent search computationally costly if not entirely infeasible. In addition, the search must consider the unknown variations in the spin frequency driven by the varying accretion rate, known as spin wandering (e.g. Mukherjee et al. 2018). The timescale of the frequency variation due to spin wandering is highly uncertain, and limits the time-span of a fully-coherent search for X-ray pulsations, and hence its achievable sensitivity.

In this paper we perform searches of X-ray data from Sco X-1 and Cyg X-2 using a semi-coherent method developed by Messenger (2011), and previously used to search for X-ray pulsations from LMXBs in Messenger & Patruno (2015) and Patruno et al. (2018). In Section 2 we outline the X-ray data selection and processing methods. In Section 3 we discuss the details of the search method and the requirements of the search. In Section 4 we report the findings of our searches. Finally in Section 6 we discuss the implications of our results and possible avenues for future work.

2 X-RAY OBSERVATIONS

The X-ray data used for Sco X-1 and Cyg X-2 were collected with the Proportional Counter Array (PCA) onboard the *Rossini X-ray Timing Explorer* (*RXTE*; Jahoda et al. 2006). The PCA consists of five identical proportional counter units (PCUs), sensitive to X-ray photons in the energy range 2–60 keV, and with a total effective area of ~ 7000 cm 2 . The instrument collects data in two “standard” modes, as well as additional user-defined data modes¹ offering different combinations of time and energy resolution. The volume of data available for both X-ray sources is very large; given that we are limited by computational cost, we select and analyse a subset of the total data available (see Section 2.3).

2.1 Observation data

The *RXTE*/PCA data were collected using a variety of datamodes. For X-ray pulsation searches, we require data modes suitable for

measuring variations in the light curve at high resolution (< 1 ms). There are three key modes we used to obtain the light curves for Sco X-1 and Cyg X-2: “EVENT” modes, “BINNED” modes and “SINGLE BIT” modes. The observation IDs of the data used for this analysis are listed in Appendix A. We used ~ 143 hr of data spanning from January 2, 1998 to Dec 26, 2010.

Since Sco X-1 is an extremely bright source ($> 10^5$ counts s $^{-1}$), modes which exceed the telemetry limit (40 kbit s $^{-1}$) result in gaps in the data. These modes are excluded from this analysis. For some observations, a unique approach was used to collect and process some of the data, involving using multiple event analyzers to collect information about events detected by different PCUs. Additionally, as reported by Jones et al. (2008), there is a significant probability of multiple detections in separate regions of the detectors, which would normally be excluded by the anti-coincidence electronics. To recover a complete time-series for Sco X-1 for the affected observations, we summed the time-series for both datamodes, as well as two counts for each of the coincident (“2-LLD”) events. This procedure required the use of DSTOOLS,² a set of data processing tools which process compressed “DS”-format files extracted from packet data obtained independently of the FITS data provided by the Guest Observer Facility.

For Cyg X-2, which is several orders of magnitude fainter than Sco X-1, we instead used the FITS data and created lightcurves using FTOOLS (Blackburn et al. 1999).

2.2 Data corrections

There are a number of factors required to correct the X-ray data to obtain the best estimate of the light curve. These factors include correcting for the motion of the Earth in the Solar System, the instrumental effects of *RXTE*'s PCA, and the deadtime. We used the JPL DE200 ephemeris to apply the barycentric corrections (Standish 1990). The instrumental effects of the PCA need to be accounted for in order to determine the count rate. These include: the offset angle from the source of the instrument, the number of proportional counter units (PCUs) in operation, and the time where the detector is not processing an event due to processing another referred to as the dead-time. These corrections are given by

$$\mu = \lambda \left(\frac{1}{1 - \theta/1 \text{ deg}} \right) \left(\frac{1}{1 - \tau_{\text{dft}}} \right) \left(\frac{1}{n_{\text{PCU}}} \right), \quad (2)$$

where μ is the best estimate of the count rate, λ is the detected count rate, θ is the offset angle in degrees, τ_{dft} is the dead-time fraction, and n_{PCU} is the number of PCUs in operation. Note that the photon detection efficiency is inversely proportional to offset angle; see Fig. 32 in Jahoda et al. (2006). The dead-time is proportional to the photon count. For Sco X-1 and Cyg X-2 the typical dead-time fractions are ~ 0.3 and ~ 0.03 respectively.

2.3 Data selection

For each LMXB we performed two complementary searches for X-ray pulsations, based on different assumptions about the spin evolution. For the first search, we assume that the spin frequency of the neutron stars have an unknown variation due to spin wandering; this constraint restricts the span of our datasets to the maximum spin-wandering timescale of the source. For the second search, we assume that spin wandering is absent (or has no effect on the spin

¹ https://heasarc.gsfc.nasa.gov/docs/xte/abc/modes_sorted.html

² E. Morgan, private communication.

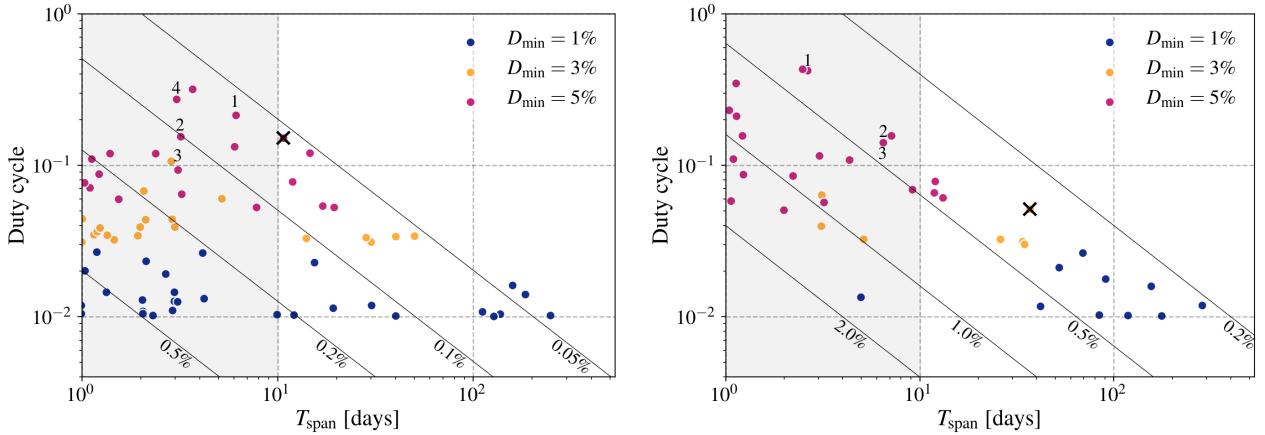


Figure 1. Duty cycle plotted against total time-span for selected subsets of *RXTE*/PCA data for Sco X-1 (left) and Cyg X-2 (right). The dots represent datasets with a set time-span and duty cycle, and the different colours represent the set duty cycle cut-off for that dataset (navy: 1%; yellow: 3%; and magenta: 5%). The black contour lines define the fractional detectable pulse amplitude. The numbers correspond to the datasets selected for searches limited to a 10 day coherence time. Properties of these datasets are listed in Tables 3 and 4. The black cross indicates the dataset selected for the search that is not limited by the coherence time. The grey shaded region corresponds to a time-span of ≤ 10 days.

frequency), and hence the spin frequency is constant. The sensitivity achieved with the latter search is constrained only by the amount of data available and the computational time.

Within a time-span T_{span} , we may find M X-ray observations of average duration T . The total on-source time nT is limited by T_{span} ; we call the ratio MT/T_{span} the duty cycle D . (For simplicity, we assume that there are no data gaps *within* each X-ray observation.) This duty cycle is typically quite small; constraints include occultation of the X-ray source by the Earth during *RXTE*'s short (~ 100 min) low-Earth orbit, times when the satellite passed through the South Atlantic Anomaly, and times when an X-ray source cannot be observed due to its proximity to the Sun. In addition, observations of X-ray sources are also generally scheduled in response to one or more observing or monitoring proposals, and not necessarily with the goal of maintaining a high duty cycle.

The relationship between the time-span T_{span} , X-ray segment duration T , duty cycle D , detectable fractional pulse amplitude A , and photon count rate μ is given by

$$A \sim 8\mu^{-1/2}(T_{\text{span}}TD)^{-1/4}. \quad (3)$$

This expression is a simplified version of that given in Messenger & Patruno (2015). Using this estimate as a guide, we calculate the detectable fractional pulse amplitude obtained for a dataset of a given time-span and duty cycle. We partition the data with a number of different cut-offs for duty cycle; for example, setting a cut-off of 1% for duty cycle would mean that each segment would have a duty cycle of at least 1%. Figure 1 shows duty cycle plotted against total time-span for selected subsets of *RXTE*/PCA data for Sco X-1 and Cyg X-2 respectively. Using these estimates, we can identify the best datasets to analyse to obtain the most sensitive search possible from the available data.³

For the first search, where we consider the effects of spin

³ Due to our simplifying assumption that there are no data gaps within each X-ray observation, the ultimate sensitivity realised by the searches may be lower by a factor of 2-4 than what is given in Fig. 1. Nevertheless, the computational cost of the search is much more sensitive to D – the duty cycle of segments within a given time-span T_{span} – than the presence of data gaps within a segment of duration $T \ll T_{\text{span}}$. Hence the assumption of no

wandering, the duration of the datasets used for the searches is limited to the calculated spin wandering timescales. Mukherjee et al. (2018) estimated the range of spin wandering timescales for Sco X-1 to be 5–80 days. Using an estimate for the accretion rate based on the luminosity, and neutron star mass and radius, we assume that the spin wandering timescales will be similar to that of Cyg X-2. We select a conservative value of 10 days for Sco X-1 and Cyg X-2. This duration is the maximum over which the variation in spin frequency can be well modelled. For the second search (assuming no spin wandering), we select the dataset that maximises the duty cycle whilst minimising the computational cost.

While Figs. 1 indicates the most sensitive datasets, they do not account for the computational cost of analysing those datasets, which may be infeasible for large T_{span} . We therefore need to make pragmatic choices of datasets which achieve almost the best sensitivity, but at significantly reduced computational cost. For example, in Fig. 1 we select datasets that does not necessarily give the smallest percentage fractional pulse amplitude A , but instead has a shorter T_{span} with a comparable value of A . This selection is made to reduce the computational cost: the difference is sensitivity between these two datasets is only a factor of ≈ 1.07 , whereas the computational cost differs by a factor > 10 . Note that the segment length T can also vary for a given dataset, and for datasets with higher duty cycles we generally have longer segments of data; from Eq. 3 we can see that we can therefore improve sensitivity by increasing T . Once datasets are selected, robust estimates of the sensitivity of each of the searches is determined using a variant of the analytic calculation given in Wette (2012).

3 SEARCH METHOD

We used a semi-coherent search method to search for X-ray pulsations from Sco X-1 and Cyg X-2. Briefly, the method partitions the X-ray data into segments of length T , performs a fully-coherent analysis of each segment, then combines results from each segment

data gaps should not noticeably affect the ranking of datasets in order to achieve the best sensitivity.

Table 1. Search parameter ranges for Sco X-1.

Parameter	Dataset	Min	Max	Units
ν	all	100	700	Hz
P_{orb}	all	68023	68024	s
a	all	1.45	3.25	lt-s
T_{asc}	1	568041816	568042347	GPS s
	2	580694264	580694775	
	3	583551268	583551775	
	4	568177864	568178394	
	no spin	600081075	600081565	

Table 2. Search parameter ranges for Cyg X-2.

Parameter	Dataset	Min	Max	Units
ν	all	100	700	Hz
P_{orb}	all	850575	850601	s
a	all	12.47	14.04	lt-s
T_{asc}	1	551418623	551421914	GPS s
	2	974156786	974168010	
	3	976708513	976719809	
	no spin	974156786	974168010	

such that the frequency evolution of the signal – though not necessarily its phase evolution – is self-consistent with a single set of parameters over the total time-span T_{span} of the search; this yields a detection statistic Σ . A detailed description of the method can be found in Messenger (2011) and Messenger & Patruno (2015). We briefly summarise parts of the search method in this section.

3.1 Signal model

X-ray pulsations from an LMXB system are modelled by a time series

$$r_j(\theta) = R\{1 + A \sin[\phi_j(\theta) + \beta]\}, \quad (4)$$

where j indexes time, $r_j(\theta)$ is the detected counts in the j th time bin, R is the expected background counts per time bin, A is the pulsed fraction of our signal, $\phi_j(\theta)$ is the signal phase, and β is a reference rotation phase of the signal. The Doppler modulation of phase $\phi_j(\theta)$ is given by

$$\phi_j(\theta) = 2\pi\nu\{t_j - t_0 - a \sin[\Omega(t_j - t_0) + \gamma]\}, \quad (5)$$

where ν is the spin frequency, t_j is the time of the j th time bin, t_0 is a reference time, a is the projected semi-major axis of the orbit, $\Omega = 2\pi/P_{\text{orb}}$ is the orbital frequency, P_{orb} is the orbital period, $\gamma = \Omega(t_0 - T_{\text{asc}})$ is the orbital phase, and T_{asc} is the time of ascension.

3.2 Parameter space

The search builds a parameter space of template waveforms to search in order to correct for the Doppler modulation due to the orbital motion of the LMXB system [Eq. (4)], which is parameterised by ν , a , Ω , and γ . For example, the amplitude of the Doppler modulation is proportional to νa , and its period is equal to P_{orb} . The volume of the parameter space is defined by the range of the orbital parameters that must be searched over; the larger the uncertainty in a parameter, the larger the volume of the parameter space.

Tables 1 and 2 list the parameter ranges for Sco X-1 (Wang et al. 2018) and Cyg X-2 (Premachandra et al. 2016) respectively. Given that the spin frequency of the target sources is unknown, we chose the range for this parameter to be 100–700 Hz. This range follows

from the assumption that the spin frequencies of these sources will lie within the current known distribution of spin frequencies for most accreting neutron star systems (Patruno et al. 2017). For all datasets the search range of the spin frequency, orbital period and projected semi-major axis remain the same. The time of ascension and its uncertainty are propagated to the epochs of the observed Sco X-1 and Cyg X-2 data; hence a value of the time of ascension is given for each dataset. The range of the time of ascension also varies for each dataset since its uncertainty grows with every orbit from the measured value.

The search method chooses template parameters (f, a, Ω, γ) at random (Messenger et al. 2009) within the ranges given in Tables 1 and 2. The templates are associated with a maximum mismatch m_{max} ; this is the maximum loss in signal-to-noise ratio that will be permitted, due to the fact that no random template will ever exactly match the parameters of the signal. Because the templates are chosen at random, the condition that the signal will be close enough to a random template to satisfy the maximum mismatch condition is guaranteed only for a fraction $\eta < 1$ of the parameter space. There is therefore a non-zero probability that the random templates do not cover some non-empty subset of the parameter space.

The number of semi-coherent templates required to obtain a fraction η of parameter-space coverage is given by

$$n = \log \left(\frac{1}{1 - \eta} \right) \frac{\pi^4 T^4 T_{\text{span}}}{25920 m_{\text{max}}^2} (\nu_{\text{max}}^4 - \nu_{\text{min}}^4) (a_{\text{max}}^3 - a_{\text{min}}^3) \times (\Omega_{\text{max}}^4 - \Omega_{\text{min}}^4) (\gamma_{\text{max}} - \gamma_{\text{min}}). \quad (6)$$

We can approximate the number of templates for Sco X-1 as

$$n \approx 6.2 \times 10^8 \left(\frac{T}{512 \text{ sec}} \right)^4 \left(\frac{T_{\text{span}}}{10 \text{ days}} \right), \quad (7)$$

and for Cyg X-2 as

$$n \approx 5.1 \times 10^6 \left(\frac{T}{512 \text{ sec}} \right)^4 \left(\frac{T_{\text{span}}}{10 \text{ days}} \right), \quad (8)$$

for a typical observation span where the mismatch $m = 0.01$, and the coverage $\eta = 0.9$. The actual number of templates used for each dataset is given in Tables 3 and 4.

4 X-RAY SEARCH RESULTS

We searched the archival *RXTE*/PCA data, prepared in Section 2, for X-ray pulsations from Sco X-1 and Cyg X-2 using the search method detailed in Section 3. No clear evidence for pulsations was found.

We present the following sets of results: searches that assume spin wandering, and hence use datasets limited to the spin wandering timescale; and searches which assume no spin wandering. Details about the properties of each dataset are provided in Tables 3, 4 and 5. These properties include: the GPS start time of each dataset t , the total on-source time within the dataset T_{obs} , the time-span of the dataset T_{span} , the total number of photons \mathcal{N} , the time-span of a single segment T , the number of segments M , the number of semi-coherent templates n , the upper limit of fractional pulse amplitude at 1% false alarm probability and 10% false dismissal probability (90% confidence) $A_{10\%}^{1\%}$, the 1% false alarm threshold on the detection statistic $\Sigma^{1\%}$, and the maximum value of the detection statistic found by the search Σ^* .

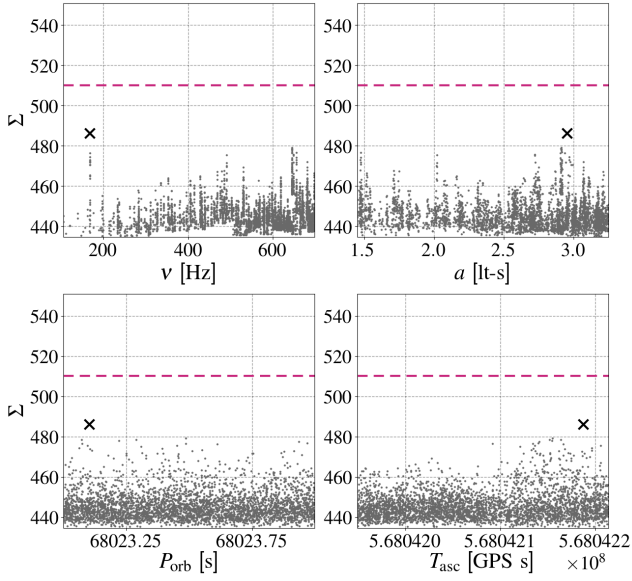


Figure 2. Detection statistic Σ plotted against the search range of frequency ν , projected semi-major axis a , period P_{orb} and time of ascension T_{asc} for dataset 1 of Sco X-1; see Table 3. The black cross indicates the template with the largest detection statistic found by the search. The dashed horizontal line at $\Sigma^{1\%} = 510.15$ indicates the 1% false alarm threshold on the detection statistic and corresponds to a fractional pulse amplitude of 0.035%. To parallelise the search, the parameter space is divided into partitions; the figure plots the 100 largest detection statistics recorded in each partition.

4.1 Assuming spin wandering

The properties of the 4 datasets searched for Sco X-1, assuming spin wandering, are given in Table 3. We set upper limits on the detectable fractional pulse amplitude of each dataset; the most stringent result for Sco X-1 is a fractional pulse amplitude of 0.035% for dataset 1. For this dataset, in Fig. 2 we plot the largest values of the detection statistic Σ found by the search against the four parameters (ν , a , P_{orb} and T_{asc}) used to define the parameter space.

The properties of the 3 datasets searched for Cyg X-2, again assuming spin wandering, are given in Table 4. The most stringent upper limit for Cyg X-2 is a fractional pulse amplitude of 0.26% for dataset 3; for this dataset, we plot in Fig. 3 the largest values of Σ against ν , a , P_{orb} and T_{asc} . The largest candidate in this dataset has $\Sigma = 207.56$, just below the 1% false alarm threshold $\Sigma^{1\%} = 207.87$; its parameters are $\nu = 695.09$ Hz, $a = 13.08$ lt-s, $P_{\text{orb}} = 850\,592.58$ s, and $T_{\text{asc}} = 976\,697\,337.62$ GPS s.

A follow-up analysis for this sub-threshold candidate following the approach of Patruno et al. (2018), where the segment time-span T is increased to improve sensitivity, is unfortunately not possible in this case. The Cyg X-2 data was not taken at 100% duty cycle, but in a series of discontinuous observations (see Appendix A). The initial search of dataset 3 used $T = 3288$ s (see Table 4), which is approximately the length of the longest observation of Cyg X-2. The semi-coherent search method used in this paper can only create one segment per observation; where T is longer than an observation, the data is zero-padded to increase resolution in the Fourier frequency domain, but does not yield increased sensitivity. Therefore, increasing T beyond that of the initial search of dataset 3 would not yield improved sensitivity, and therefore we are unable to perform a follow-up search for the candidate. Nevertheless, we

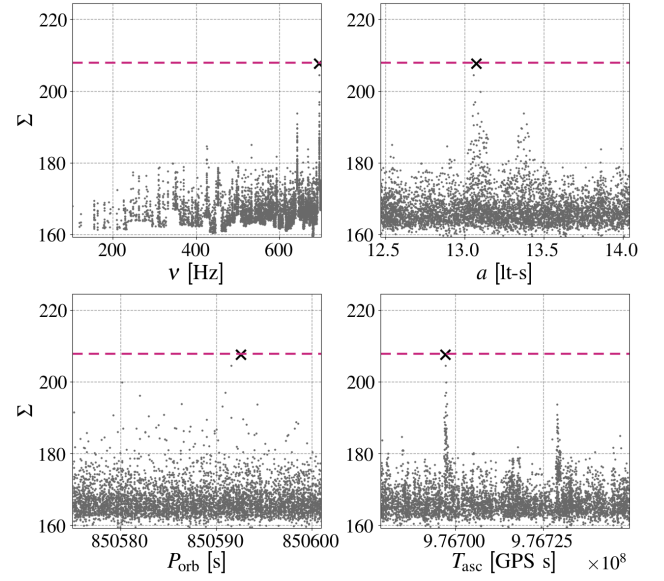


Figure 3. Same as Fig. 2, but for dataset 3 of Cyg X-2; see Table 4. The dashed horizontal line at $\Sigma^{1\%} = 207.87$ indicates the 1% false alarm threshold on the detection statistic and corresponds to a fractional pulse amplitude of 0.26%.

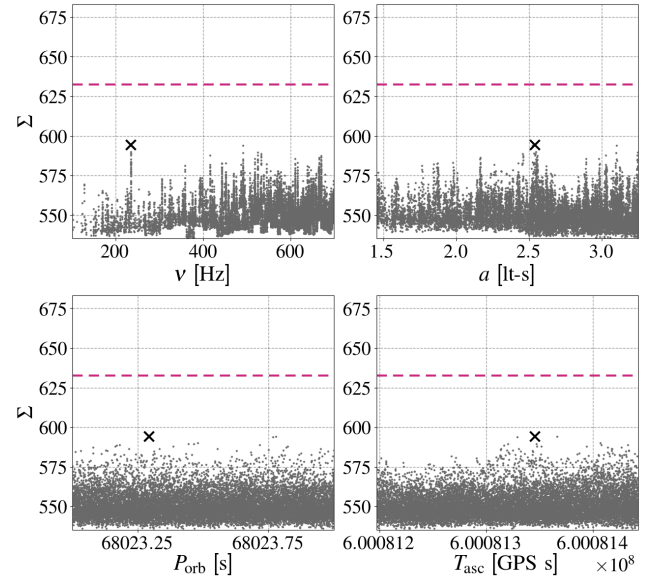


Figure 4. Detection statistic Σ plotted against the search range of frequency ν , projected semi-major axis a , period P_{orb} and time of ascension T_{asc} for a search for Sco X-1 assuming no spin wandering; see Table 5. The black cross indicates the template with the largest detection statistic found by the search. The dashed horizontal line at $\Sigma^{1\%} = 632.59$ indicates the 1% false alarm threshold on the detection statistic and corresponds to a fractional pulse amplitude of 0.034%. The 100 largest detection statistics recorded in each parameter space partition are plotted.

Table 3. Data parameters, estimated sensitivities, and upper limits for Sco X-1. Columns are: dataset number, GPS start time of dataset, total on-source time within the dataset, time-span of dataset, number of photons, time-span of a single segment, number of segments, number of semi-coherent templates, upper limit of fractional pulse amplitude at 1% false alarm probability and 10% false dismissal probability (90% confidence), 1% false alarm threshold on the detection statistic, largest value of detection statistic found by the search.

No.	t [GPS s]	$T_{\text{obs}}/10^5$ [s]	$T_{\text{span}}/10^5$ [s]	$N/10^9$	T [s]	M	$n/10^9$	$A_{10\%}^{1\%}$	$\Sigma^{1\%}$	Σ^*
1	567787966	0.89	5.45	3.17	528	153	4.95	0.035%	510.15	486.06
2	580523651	0.46	2.82	1.50	697	55	10.63	0.036%	248.78	230.08
3	583396353	0.30	2.73	1.01	579	46	6.24	0.041%	220.22	197.31
4	613041597	0.61	2.65	1.45	699	77	10.99	0.041%	311.79	297.13

Table 4. Data parameters, estimated sensitivities, and upper limits for Cyg X-2. Columns are as for Table 3.

No.	t [GPS s]	$T_{\text{obs}}/10^5$ [s]	$T_{\text{span}}/10^5$ [s]	$N/10^6$	T [s]	M	$n/10^9$	$A_{10\%}^{1\%}$	$\Sigma^{1\%}$	Σ^*
1	551735827	0.60	2.33	3.64	2402	30	38.28	0.61%	175.80	155.43
2	974186811	0.78	5.65	21.39	2111	39	52.79	0.27%	205.64	195.56
3	976792264	0.73	5.91	24.57	3288	40	39.76	0.26%	207.87	207.56

Table 5. Data parameters, estimated sensitivities, and upper limits assuming no spin wandering. Columns are as for Table 3, except that column 1 lists the source name.

Source	t [GPS s]	$T_{\text{obs}}/10^5$ [s]	$T_{\text{span}}/10^5$ [s]	$N/10^9$	T [s]	M	$n/10^9$	$A_{10\%}^{1\%}$	$\Sigma^{1\%}$	Σ^*
Sco X-1	599635471	1.50	9.27	4.25	707	199	16.71	0.034%	632.59	594.18
Cyg X-2	974186811	1.51	31.97	0.05	3499	79	46.97	0.23%	322.97	290.40

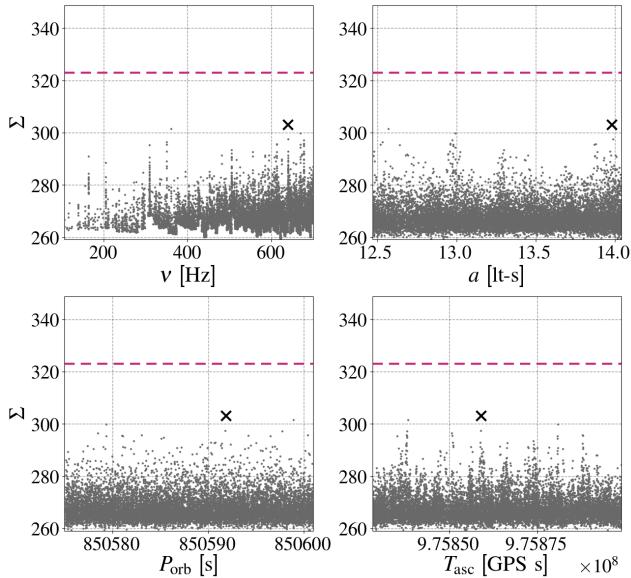


Figure 5. Same as Fig. 4 but for Cyg X-2. The dashed horizontal line at $\Sigma^{1\%} = 322.97$ indicates the 1% false alarm threshold on upper limit and corresponds to a fractional pulse amplitude of 0.23%.

note that the Fig. 3 shows features which disfavour the presence of a signal; the candidate is unresolved in the P_{orb} parameter space (compare the lower left panel to that of Fig. 6) and similar, only slightly smaller peaks appear at different values of a and T_{asc} (right-hand panels). Finally, the analysis of a neighbouring segment of data (dataset 2, see Fig. B5) did not yield a strong candidate at these parameters.

The results of searches of the other Sco X-1 and Cyg X-2 datasets listed in Tables 3 and 4 are given in Appendix B.

Table 6. Simulated and recovered best-match parameters for the simulated search.

Parameter	Simulated	Recovered	Units
ν	502.4000 ± 0.0001 (95%)	502.40	Hz
P_{orb}	[68023, 68024]	68023.4	s
a	2.750 ± 0.003 (95%)	2.744	lt-s
T_{asc}	600081300 ± 20 (95%)	600081290	GPS s
A	693.21 ± 74.47 (95%)	629.44	-

4.2 Assuming no spin wandering

We also performed searches for each source assuming no spin wandering. The most sensitive searches were limited by computational cost and achieved fractional pulse amplitude upper limits of 0.034% for Sco X-1 (Fig. 4) and 0.23% for Cyg X-2 (Fig. 5). These searches gave the most stringent upper limits on the detectable fractional pulse amplitude for the respective sources.

5 RECOVERY OF A SIMULATED SIGNAL

To illustrate the recovery of X-ray pulsations at the very limit of search sensitivity, we performed a search of an simulated dataset. The dataset has similar properties to the Sco X-1 dataset with no spin wandering, including the time-span, duty cycle, background photon count rate. It also contains a simulated signal, generated using the signal model described by Eq. 4, with a fractional pulse amplitude of 0.034%. The frequency and orbital parameters of the simulated signal are randomly chosen from the Sco X-1 parameter ranges given in Table 1.

The simulated signal is just recovered at the 1% false alarm threshold, as shown in Fig. 6, demonstrating that the method can detect signals with the claimed fractional pulse amplitude of 0.034% at 90% confidence. The frequency and projected semi-major axis parameters of the recovered signal are clearly constrained. The uncertainties in orbital period and time of ascension from observations are small enough, however, that the search does not provide tighter constraints. The parameters of the simulated signal and of the recov-

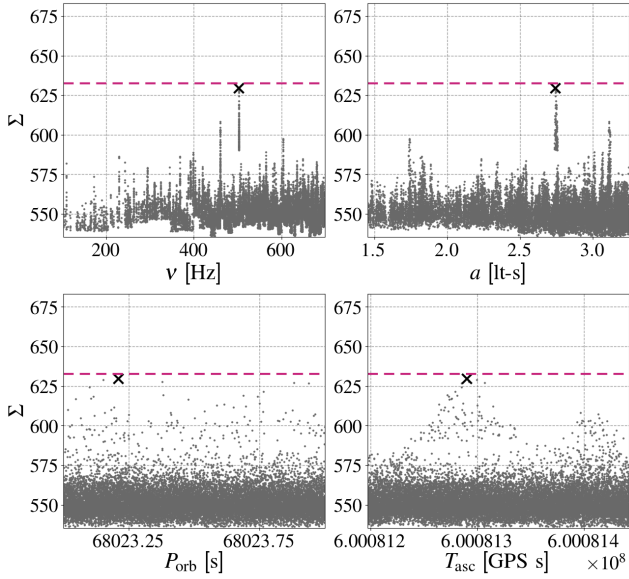


Figure 6. Detection statistic Σ plotted against the search range of frequency ν , projected semi-major axis a , period P_{obs} and time of ascension T_{asc} for a simulated dataset, with similar properties to the Sco X-1 dataset with no spin wandering, and containing a signal with a fractional pulse amplitude of 0.034%. The black cross indicates the template with the largest detection statistic found by the search. The dashed horizontal line at $\Sigma^{1\%} = 632.59$ indicates the 1% false alarm threshold on the detection statistic and corresponds to the same fractional pulse amplitude as the simulated signal. The 100 largest detection statistics recorded in each parameter space partition are plotted.

ered best-match template are given in Table 6. The recovered signal is not identical to the simulated signal; this discrepancy is expected since there is a loss of signal-to-noise ratio due to the mismatch between the signal and (random) template parameters.

6 DISCUSSION

We conducted a semi-coherent search for X-ray pulsations on archival *RXTE*/PCA data for Sco X-1 and Cyg X-2 with a total on-source observation time of ~ 104.4 hr and ~ 48.5 hr respectively. We perform a set of searches assuming that the spin wandering timescale limits the length of the coherently-analysed segments, and an additional set assuming no restrictions due to spin wandering. We detected no clear evidence of persistent X-ray pulsations, and found the most stringent upper limits (at 90% confidence) on the fractional pulse amplitude to be 0.034% for Sco X-1 and 0.23% for Cyg X-2.

Vaughan et al. (1994) performed fully-coherent searches of 1024–2048 s observations taken by the Large Area Counter onboard the *Ginga* satellite, and set best upper limits (at 99% confidence) of 0.28% on Sco X-1 and 0.37% on Cyg X-2. The time-spans of the coherent searches in Vaughan et al. (1994) are comparable to the coherent segment lengths of our searches for Cyg X-2 (Table 4), and up to a factor of ~ 3.5 greater than those of our searches for Sco X-1 (Table 3). On the other hand, our semi-coherent searches analyse ~ 29 times more than data in total than a single coherent analysis of Vaughan et al. (1994), and moreover combine coherent segments together for improved sensitivity. Taken together with the improved sensitivity of *RXTE* compared to *Ginga* – ~ 0.17 mCrab (Jahoda

et al. 2006) versus ~ 0.2 mCrab (Turner et al. 1989) – our upper limits on Sco X-1 and Cyg X-2 improve upon those of Vaughan et al. (1994) by factors of ~ 8.2 and ~ 1.6 respectively.

The non-detection of X-ray pulsations from Sco X-1 and Cyg X-2, presented in this paper, is consistent with null results from other pulsation searches for LMXBs (e.g. Messenger & Patruno 2015; Patruno et al. 2018). The absence of observed pulsations from many LMXBs might be due to a number of factors:

(i) Weak magnetic fields that do not channel matter would present a possible explanation for the absence of pulsations (Cumming et al. 2001). Some LMXBs such as Aquila X-1, however, exhibit strong transient pulsations (Casella et al. 2008; Messenger & Patruno 2015), which would require a momentary increase in the magnetic field strength inconsistent with this model.

(ii) Pulsations may be present but not persistent. Some neutron stars are known to intermittently exhibit X-ray pulsations (Galloway et al. 2007). The semi-coherent search method used in this paper is designed for persistent signals, and would be unlikely to detect pulsations that are both weak and intermittent.

(iii) Pulsations may be suppressed by electron scattering in the optically thick material surrounding the LMXB (Titarchuk et al. 2002; Göğüş et al. 2007), and therefore may be too weak to be detectable with current data analysis techniques, or else absent altogether.

(iv) Sco X-1 may not be a neutron star, in which case we would not expect X-ray pulsations.

Future searches for X-ray pulsations from Sco X-1, Cyg X-2, and other LMXBs could make use of improved data analysis methods that e.g. permit longer segments of data to be analysed coherently. In addition, future X-ray satellite missions such as STROBE-X (Ray et al. 2018) may provide more sensitive X-ray data to search for X-ray pulsations and thereby support the search for continuous gravitational waves.

ACKNOWLEDGEMENTS

This research was conducted by the Australian Research Council Centre of Excellence for Gravitational Wave Discovery (OzGrav), through project number CE170100004. The authors also gratefully acknowledge the Science and Technology Facilities Council of the United Kingdom. CM is supported by the Science and Technology Research Council (grant No. ST/L000946/1). This research has made use of data and software provided by the High Energy Astrophysics Science Archive Research Center (HEASARC), which is a service of the Astrophysics Science Division at NASA/GSFC and the High Energy Astrophysics Division of the Smithsonian Astrophysical Observatory. The searches for X-ray pulsations were performed on the OzSTAR national facility at Swinburne University of Technology. OzSTAR is funded by Swinburne University of Technology and the National Collaborative Research Infrastructure Strategy (NCRIS).

DATA AVAILABILITY

The data used in this paper was processed from data provided by the High Energy Astrophysics Science Archive Research Center (HEASARC). Links to processed data and result files can be found at: https://github.com/shanikagalaudage/xray_pulsations

REFERENCES

- Aasi J., et al., 2015a, *Class. Quant. Grav.*, **32**, 074001
- Aasi J., et al., 2015b, *Phys. Rev. D*, **91**, 062008
- Abbott B., et al., 2007a, *Phys. Rev. D*, **76**, 082001
- Abbott B., et al., 2007b, *Phys. Rev. D*, **76**, 082003
- Abbott B. P., et al., 2017a, *Phys. Rev. D*, **95**, 122003
- Abbott B. P., et al., 2017b, *Phys. Rev. Lett.*, **118**, 121102
- Abbott B. P., et al., 2017c, *ApJ*, **847**, 47
- Abbott B. P., et al., 2019a, *Phys. Rev. D*, **100**, 122002
- Abbott B. P., et al., 2019b, *Phys. Rev. D*, **100**, 062001
- Acernese F., et al., 2015, *Class. Quant. Grav.*, **32**, 024001
- Bildsten L., 1998, *ApJ*, **501**, L89
- Blackburn J. K., Shaw R. A., Payne H. E., Hayes J. J. E., Heasarc 1999, FTOOLS: A general package of software to manipulate FITS files (ascl:9912.002)
- Casella P., Altamirano D., Patruno A., Wijnands R., van der Klis M., 2008, *ApJ*, **674**, L41
- Chakrabarty D., Morgan E. H., Munro M. P., Galloway D. K., Wijnands R., van der Klis M., Markwardt C. B., 2003, *Nature*, **424**, 42
- Cook G. B., Shapiro S. L., Teukolsky S. A., 1994, *ApJ*, **423**, L117
- Cumming A., Zwebel E., Bildsten L., 2001, *ApJ*, **557**, 958
- Damle S. V., Kunte P. K., Leahy D. A., Naranan S., Sreekantan B. V., Venkatesan D., 1988, *Adv. Space Res.*, **8**, 415
- Galloway D. K., Morgan E. H., Krauss M. I., Kaaret P., Chakrabarty D., 2007, *ApJ*, **654**, L73
- Göğüş E., Alpar M. A., Gilfanov M., 2007, *ApJ*, **659**, 580
- Jahoda K., Markwardt C. B., Radeva Y., Rots A. H., Stark M. J., Swank J. H., Strohmayer T. E., Zhang W., 2006, *ApJS*, **163**, 401
- Jones T. A., Levine A. M., Morgan E. H., Rappaport S., 2008, *ApJ*, **677**, 1241
- Leaci P., Prix R., 2015, *Phys. Rev. D*, **91**, 102003
- Manchanda R. K., 2005, in 29th International Cosmic Ray Conference (ICRC29), Volume 4. p. 183
- Meadors G. D., Goetz E., Riles K., Creighton T., Robinet F., 2017, *Phys. Rev. D*, **95**, 042005
- Messenger C., 2011, *Phys. Rev. D*, **84**, 083003
- Messenger C., Patruno A., 2015, *ApJ*, **806**, 261
- Messenger C., Prix R., Papa M. A., 2009, *Phys. Rev. D*, **79**, 104017
- Middleton H., Clearwater P., Melatos A., Dunn L., 2020, *Phys. Rev. D*, **102**, 023006
- Mukherjee A., Messenger C., Riles K., 2018, *Phys. Rev. D*, **97**, 043016
- Papaloizou J., Pringle J. E., 1978, *MNRAS*, **184**, 501
- Patruno A., Haskell B., Andersson N., 2017, *ApJ*, **850**, 106
- Patruno A., Wette K., Messenger C., 2018, *ApJ*, **859**, 112
- Premachandra S. S., Galloway D. K., Casares J., Steeghs D. T., Marsh T. R., 2016, *ApJ*, **823**, 106
- Prix R., 2009, in Becker W., ed., *Astrophysics and Space Science Library* Vol. 357, Neutron Stars and Pulsars. Springer, Berlin/Heidelberg, p. 651, doi:10.1007/978-3-540-76965-1_24
- Ray P. S., et al., 2018, in Proc. SPIE. p. 1069919 (arXiv:1807.01179), doi:10.1117/12.2312257
- Standish Jr. E. M., 1990, *A&A*, **233**, 252
- Titarchuk L., Cui W., Wood K., 2002, *ApJ*, **576**, L49
- Turner M. J. L., et al., 1989, *PASJ*, **41**, 345
- Van Den Broeck C., 2005, *Class. Quant. Grav.*, **22**, 1825
- Vaughan B. A., et al., 1994, *ApJ*, **435**, 362
- Wagoner R. V., 1984, *ApJ*, **278**, 345
- Wang L., Steeghs D., Galloway D. K., Marsh T., Casares J., 2018, *MNRAS*, **478**, 5174
- Watts A. L., Krishnan B., Bildsten L., Schutz B. F., 2008, *MNRAS*, **389**, 839
- Wette K., 2012, *Phys. Rev. D*, **85**, 042003
- Wood K. S., et al., 1991, *ApJ*, **379**, 295

Table A1. Observation IDs for Scorpius X-1

Dataset	Observation IDs	Duty Cycle (%)
1	10061-01-03-00, 20053-01-02-00, 20053-01-02-01, 20053-01-02-02, 20053-01-02-03, 30036-01-01-00, 20053-01-02-04, 20053-01-02-05, 30036-01-02-00	16.34
2	30035-01-01-00, 30035-01-02-00, 30035-01-05-00, 30035-01-03-00, 30035-01-06-00, 30035-01-04-00	16.15
3	30035-01-07-00, 30035-01-08-00, 30035-01-11-00, 30035-01-09-00, 30035-01-10-00	11.09
4	40706-02-01-00, 40706-02-03-00, 40706-02-06-00, 40706-01-01-00, 40706-02-09-00, 40706-02-08-00, 40706-02-10-00, 40706-02-12-00, 40706-02-13-00, 40706-02-14-00, 40706-01-02-00, 40706-02-16-00, 40706-02-17-00, 40706-02-18-00, 40706-02-19-00, 40706-02-21-00, 40706-02-22-00, 40706-02-23-00, 40706-01-03-00	22.84
no spin	40020-01-02-00, 40020-01-01-00, 40020-01-01-01, 40020-01-01-02, 40020-01-01-03, 40020-01-01-04, 40020-01-01-05, 40020-01-01-06, 40020-01-01-07, 40020-01-03-00, 40020-01-03-01	16.19

Table A2. Observation IDs for Cygnus X-2

Dataset	Observation IDs	Duty Cycle (%)
1	20053-04-01-00, 20053-04-01-01, 20053-04-01-02, 20053-04-01-06, 20053-04-01-03, 20053-04-01-04, 20053-04-01-07, 20053-04-01-05	25.98
2	95345-01-01-00, 95345-01-02-00, 95345-01-02-01, 95345-01-03-00, 95345-01-04-00, 95345-01-05-00, 95345-01-06-01, 95345-01-06-00, 95345-01-07-00, 95345-01-08-00, 95345-01-08-01, 95345-01-09-00, 95345-01-10-00, 95345-01-11-00, 95345-01-12-00, 95345-01-13-00, 95345-01-14-00, 95345-01-15-00, 95345-01-16-00, 95345-01-17-00, 95345-01-18-00, 95345-01-19-00, 95345-01-20-00, 95345-01-21-00	13.75
3	95345-01-22-00, 95345-01-23-00, 95345-01-23-01, 95345-01-24-00, 95345-01-25-00, 95345-01-26-00, 95345-01-26-01, 95345-01-27-00, 95345-01-28-00, 95345-01-29-00, 95345-01-29-01, 95345-01-30-00, 95345-01-31-00, 95345-01-32-00, 95345-01-32-02, 95345-01-33-00, 95345-01-34-00, 95345-01-34-01, 95345-01-35-02, 95345-01-35-01, 95345-01-36-00, 95345-01-37-00, 95345-01-37-01, 95345-01-38-00, 95345-01-38-01, 95345-01-39-00, 95345-01-40-01	12.3
no spin	Datasets 2 and 3	4.71

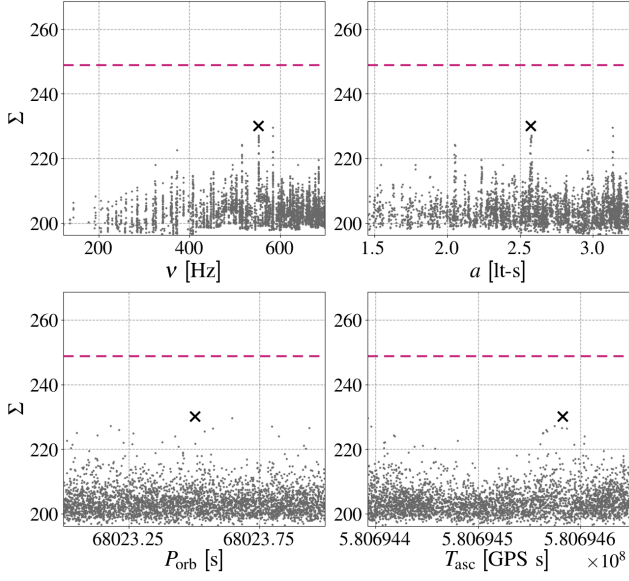


Figure B1. Results for Sco X-1 dataset 2: $\Sigma^{1\%} = 248.78$.

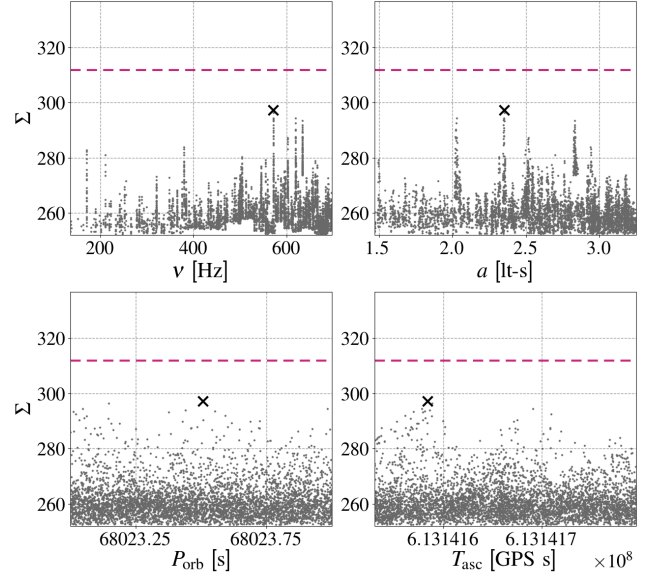


Figure B3. Results for Sco X-1 dataset 4: $\Sigma^{1\%} = 311.79$.

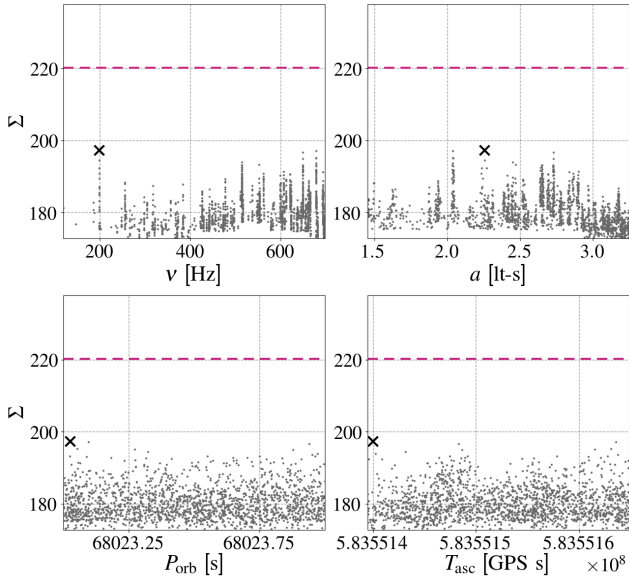


Figure B2. Results for Sco X-1 dataset 3: $\Sigma^{1\%} = 220.22$.

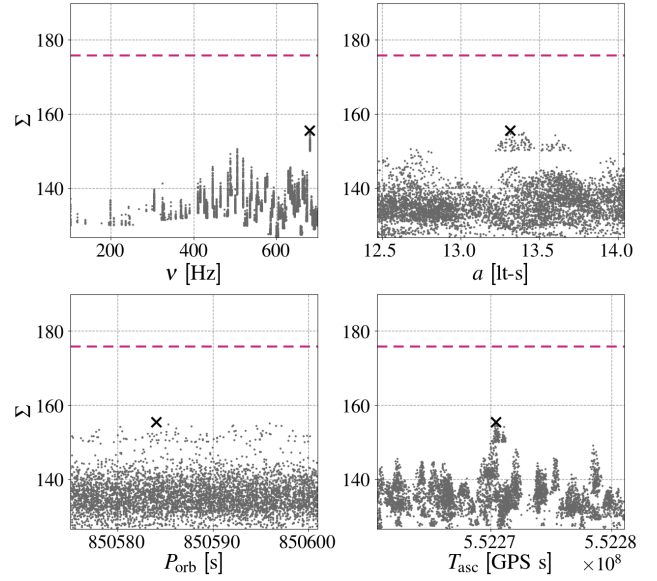


Figure B4. Results for Cyg X-2 dataset 1: $\Sigma^{1\%} = 175.80$.

APPENDIX A: DATASET OBSERVATION IDS

Tables A1 and A2 list the observation IDs for the Sco X-1 and Cyg X-2 datasets, respectively, that were analysed in this paper. The duty cycle is the measured as the percentage exposure time over the total time span of the observation set.

APPENDIX B: ADDITIONAL SCO X-1 AND CYG X-2 SEARCHES

In this section we present the results from the additional datasets analysed. For each figure we plot the detection statistic Σ against the search range of frequency ν , projected semi-major axis a , period

P_{obs} and time of ascension T_{asc} . The black cross indicates the template with the largest detection statistic found by the search (Σ^*). The dashed horizontal line indicates the 1% false alarm threshold on the detection statistic ($\Sigma^{1\%}$). The 100 largest detection statistics recorded in each parameter space partition are plotted.

This paper has been typeset from a $\text{\TeX}/\text{\LaTeX}$ file prepared by the author.

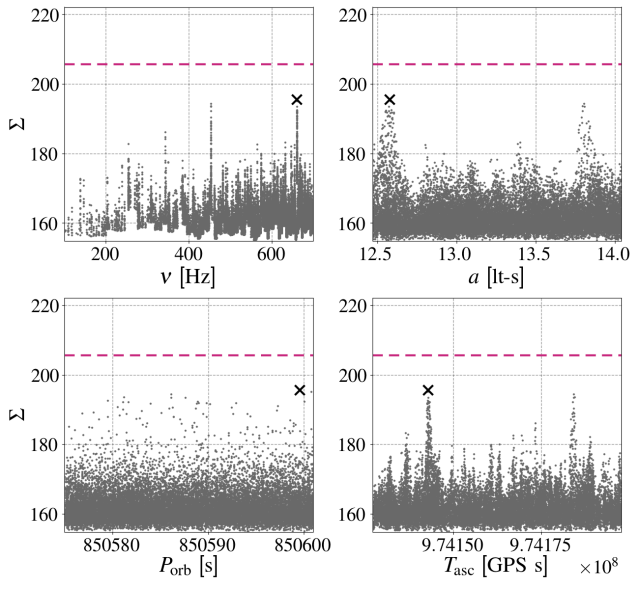


Figure B5. Results for Cyg X-2 dataset 2: $\Sigma^{1\%} = 279.57$.